Journal of Alloys and Compounds 611 (2014) 104–110

Contents lists available at ScienceDirect

Journal of Alloys and Compounds

journal homepage: www.elsevier.com/locate/jalcom

Microstructural characteristics of the microphase Y-Ti_2SC in nickel-based superalloys

X.B. Hu, Y.B. Xue, S.J. Zheng, Y.L. Zhu, D. Chen, X.L. Ma *

Shenyang National Laboratory for Materials Science, Institute of Metal Research, Chinese Academy of Sciences, Shenyang 110016, China

ARTICLE INFO

Article history:
Received 13 March 2014
Received in revised form 14 May 2014
Accepted 15 May 2014
Available online 23 May 2014

Keywords:
Ni-based superalloys
Transmission electron microscopy
Y-Ti_2SC phase
MC-type carbide
Interface

ABSTRACT

The microstructural characteristics of microphase Y-Ti_2SC in Ni-based superalloys have been studied by means of analytical transmission electron microscopy (TEM). In the standard heat treated samples, the Y phase always exhibits slab morphology forming either the sandwiched plate in MC or the side-by-side structure with MC. Moreover, the Y phase also maintains an definite crystallographic orientation relationship of $[1\bar{2}10]_Y//[1\bar{1}0]_{MC}$ and $(0001)_Y//(111)_{MC}$ with the MC-type carbide. Stacking fault which results from the insertion of two Ti–C layers has been identified in the Y-Ti_2SC phase. Combined with high resolution TEM (HRTEM) and first-principles calculations, we also determine the most stable interfacial structure between Y phase and MC carbide. Additionally, we find that Y-Ti_2SC phase can solutionize amounts of beneficial elements Hf and Zr from the matrix during long-term annealing process, which leads to its lattice expansion. This solution phenomenon is detrimental for superalloys due to the consumption of the beneficial elements.

1. Introduction

Due to impurity of raw material and possible contamination during metallurgical process, trace amounts (ppm) of sulfur in the cast alloy is always uncontrollable. Besides that, sulfur can also be easily introduced into the superalloys surface in variety of post-casting treatments, such as the commonly seen grift blasting [1]. But no matter introduced in which step, the impurity sulfur is recognized as a harmful element for superalloys, which not only reduces the grain/phase boundary energy due to element segregation [2–5], but also plays detrimental roles in the solidification process [6–9]. Furthermore, the impurity sulfur can also cause oxidation resistance to be degraded by deteriorating thermal barrier coating (TBC) adherence [10,11]. In addition to segregation at grain/phase boundaries, sulfur can also distribute in MC-type (M represents transition metal such as Ti, Ta and Hf) carbide or form the Y phase with chemical composition of Ti_2SC [12]. The Ti_2SC phase ($P6_3/mmc$, $a = 0.32$ nm, $c = 1.122$ nm), as a layered machinable ternary carbide, has the significantly shorter c-lattice compared with most of members in the $M_{n+1}AX_n$ (MAX) phase family (M = early transition metal; A = A group element and X = C or N and $n = 1–3$) to which it belongs [13]. In particular, among the known M_2AX serial phases, the c-lattice of Ti_2SC is 24.88% less than that of the largest one Zr_2InC ($P6_3/mmc$, $a = 0.32$ nm, $c = 1.491$ nm). Although there is no definite relationship between the mechanical properties and length of the c-lattice, it is speculated that the properties of Ti_2SC might be significantly different from other MAX phases [14–17]. The bulk sample can be synthesized by hot pressing Ti_2SC powder [18] or in situ/hot press method [19]. And experiments conform that Young's modulus for bulk Ti_2SC is one of the highest for M_2AX phases [20]. Moreover, bulk Ti_2SC also exhibits the highest room temperature thermal conductivity [21] and the lowest Poisson's ratio [22] as compared to other MAX phases.

However, the so-called MAX phase Ti_2SC is considered as a deleterious phase in superalloys, which decreases the tensile and stress-rupture properties [12]. The volume fraction of Y-Ti_2SC increases with the content of impurity sulfur. All these deleterious effects are proposed to be closely related with its microstructural features although which have not been understood well [12,23]. In other aspects, the knowledge on Y-Ti_2SC phase acquired from the literatures is just at a micrometer scale. Therefore, some fine structural characteristics remain unclarified due to the limitation of resolution. So, an accurate understanding for the microstructures of Y-Ti_2SC phase is needed to improve the comprehensive cognition of ceramic MAX phase Ti_2SC, as well as superalloys.

* Corresponding author. Tel.: +86 24 23971845.
E-mail address: xlma@imr.ac.cn (X.L. Ma).

http://dx.doi.org/10.1016/j.jallcom.2014.05.104
0925-8388/

2. Experimental procedures

Chemical composition of the nickel-based superalloy used in this work is as follows (in wt.%): 15.5 Cr, 10.8 Co, 2.1 Mo, 5.6 W, 3.2 Al, 4.6 Ti, 0.2 Nb, 0.1 Ta, 0.4 Hf, 0.04 Zr, 0.073 C, 0.075 B, 0.0008 S and balance Ni. First, we performed standard heat treatment on the alloy. The as-cast alloy was subjected to solution treatment at 1170 °C for 4 h followed by air-cooling. Subsequently, the two-step ageing treatment was utilized. Primary precipitate aging treatment was carried out at 1050 °C for 4 h followed by air-cooling, and the secondary was conducted at 850 °C for 16 h followed by air-cooling too. Then, parts of the standard heat treated samples were annealed at 900 °C for 1000 h and cooled in air for investigating the morphology, composition and structural evolution of precipitated phase.

Transmission electron microscopy (TEM) foils were prepared by cutting, grinding and dimpling, followed by ion-milling in the Gatan precision ion polishing system (PIPS) with a liquid-nitrogen-cooled stage for avoiding preferential thinning effects. The Tecnai G^2 F30 transmission electron microscope, equipped with a high-angle annular dark-field (HAADF) detector, X-ray energy-dispersive spectrometer (EDS) systems, operated at 300KV, was used for microstructural and compositional investigations. A Fischione plasma cleaner was used before acquiring composition analysis to remove surface pollution. The dead time for the EDS acquisition is approximate 25%. During the EDS line-scan measurements, a sub-nanometer probe (approximately 0.3 nm in diameter) with a step of 3 nm was applied. Using the commercial JEMS software, image simulation was performed to determine the atomic positions.

All calculations were carried out with the Vienna Ab initio Simulation Package (VASP) [24,25] in the framework of density functional theory (DFT). The projector-augmented wave (PAW) method [26,27] was applied to describe the core-valence electron interaction and the generalized gradient approximation (GGA) formulated by Perdew, Burke and Ernzerhof (PBE) [28] was employed to treat the exchange correlation between electrons. The plane-wave cutoff energy was set at 450 eV and the Monkhorst–Pack scheme [29] was used for the k-point sampling.

3. Results and discussion

3.1. Morphology, composition and structure of Y phase

The TEM micrographs shown in Fig. 1a and b display the MC-type carbide precipitates in the matrix (included γ/γ' phase) obtained from the standard heat treated samples. And the inset electron diffraction pattern (EDP) in Fig. 1a and the inset EDP in Fig. 1b correspond to the matrix and MC phase, respectively. Moreover, there are distinct contrast inside the MC carbide as shown in Fig. 1a and along the interface between MC and matrix as seen in Fig. 1b. Considering the knowledge obtained from literatures that the coexistence of MC and Y-Ti_2SC phase is possible [12], the above distinct contrast should correspond to the Y-Ti_2SC phase. To clarify the contrast characteristic along the interface between MC and matrix, the locally magnified image of Fig. 1b (dark-field image obtained by using a coincident reflection from the MC carbide and the Y phase) is shown in Fig. 1c. Since sulfur was not added in our alloying, the Y phase with minor volume fraction is proposed to result from an unavoidable element impurity. Based on our TEM observation as shown in Fig. 1, there are two types of positional characteristics for Y-Ti_2SC phase. The first positional characteristic is the sandwiched structure with Y phase precipitate (indicated by solid arrow) inside MC carbide as shown in Fig. 1a. The second positional characteristic is the side-by-side structure as shown in Fig. 1b. The generation of above special positional characteristics should be ascribed to the uneven distribution of sulfur in the MC-type carbides formed as the alloy was casted [8]. On account of our experimental results, it is reasonable to deduce that the standard heat treating leads sulfur to distributing regularly. When sulfur segregates mainly inside MC carbide, the sandwiched structure could form. Similarly, segregation of sulfur at the edge of the MC carbide results in the formation of side-by-side structure.

Fig. 2a is a typical HAADF image displaying the side-by-side structure of Y phase and MC-type carbide, which was acquired from the standard heat treated samples. To have chemical information around this precipitate, we performed EDS line-scan across the Y phase, MC, and the matrix along the solid red line denoted in Fig. 2a. The results displayed in Fig. 2b demonstrate that Y phase is composited by C, S, and Ti primarily. The content fluctuation of Ni clearly exhibits the boundaries between the matrix and the side-by-side structure. The boundaries among different phases are highlighted by the dot lines in Fig. 2b. As a result of lack in heavier elements compared with the MC (M = Ti, Ta) carbide and the matrix, Y phase presents the darkest contrast in this imaging mode.

Fig. 3a–c shows selected-area electron diffraction (SAED) patterns of hexagonal Y phase, which are obtained from several zone-axes via large-angle tilting along $[0001]_Y$ direction and can be indexed as $[1\bar{2}10]_Y$, $[4\bar{5}10]_Y$, and $[1\bar{1}00]_Y$ zone-axis, respectively. Tilting the grain from $[1\bar{2}10]_Y$ zone axis as shown in Fig. 3a about 19°, $[4\bar{5}10]_Y$ zone is acquired as shown in Fig. 3b. And continuing tilting about 11°, $[1\bar{1}00]_Y$ zone axis is acquired as shown in Fig. 3c. Based on the above electron diffraction patterns (EDPs), the lattice parameters can be derived as $a = 0.33$ nm, $c = 1.15$ nm. Due to the existence of microcosmic symmetry for Y phase, structural extinction can happen. For example, on account of the c glide plane perpendicular to the $[1\bar{1}00]_Y$ crystallographic direction, $(\mathbf{hh\bar{2}hl})_Y$ reflection is non-existent in the EDPs when l = odd, as shown in Fig. 3c. In a similar way, $(0001)_Y$ reflection should vanish when l = odd in EDPs because of 6_3 screw axis along $[0001]_Y$ crystallographic direction, as seen in Fig. 3b.

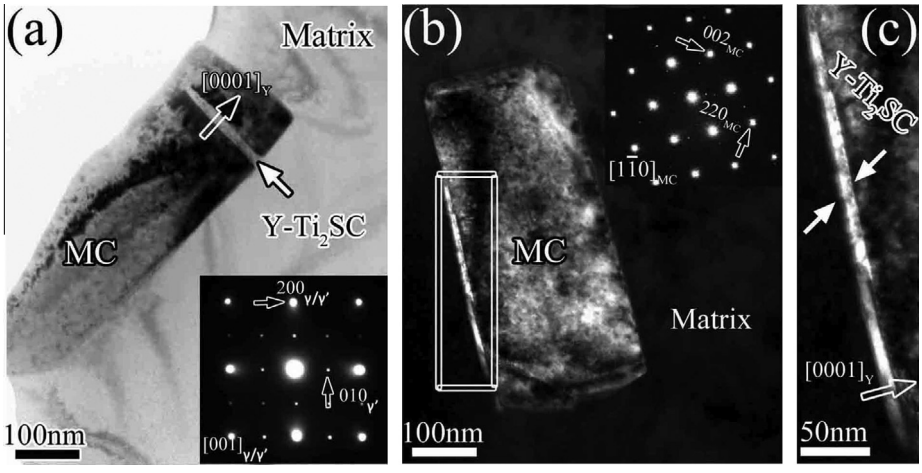

Fig. 1. (a) Bright field (BF) image of Y phase with sandwiched structure and (b) dark field (DF) image of Y phase with side-by-side structure obtained from the standard heat treated sample, and (c) a locally magnified image of the frame in (b). The bottom-right electron diffraction pattern (EDP) in (a) and top-right EDP in (b) correspond to $[001]_{\gamma/\gamma'}$ and $[1\,1\,0]_{MC}$ zone-axis respectively. The $[0\,0\,0\,1]_Y$ direction for Y phase is indicated by the hollow arrow.

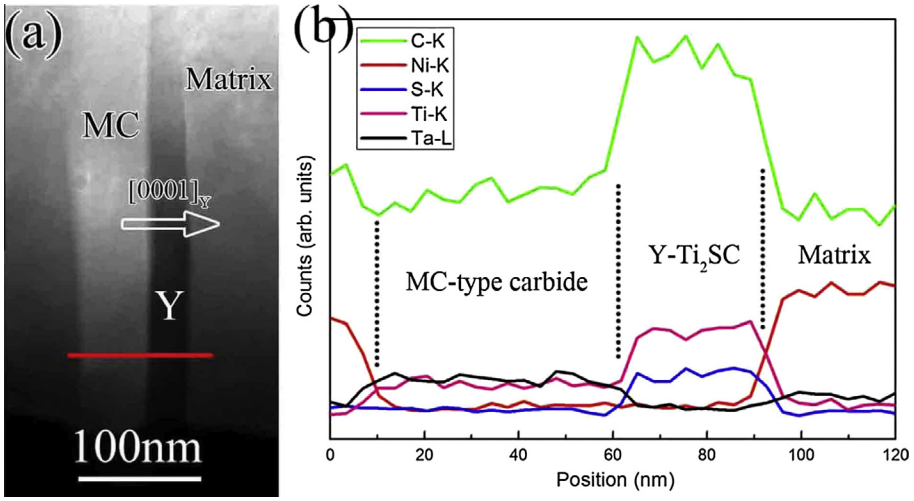

Fig. 2. (a) HAADF image including Y-Ti_2SC phase, MC (M = Ti, Ta) carbide and the matrix obtained from the standard heat treated samples. The hollow arrow indicates the $[0001]_Y$ direction for Y phase and (b) EDS line-scan profiles scanned along the red line in (a). The profiles corresponding to the elements of C, Ni, S, Ti and Ta, indicated by green, red, blue, pink and black colors, respectively. The corresponding location for matrix, Y-Ti_2SC and MC phase are indicated. (For interpretation of the references to colour in this figure legend, the reader is referred to the web version of this article.)

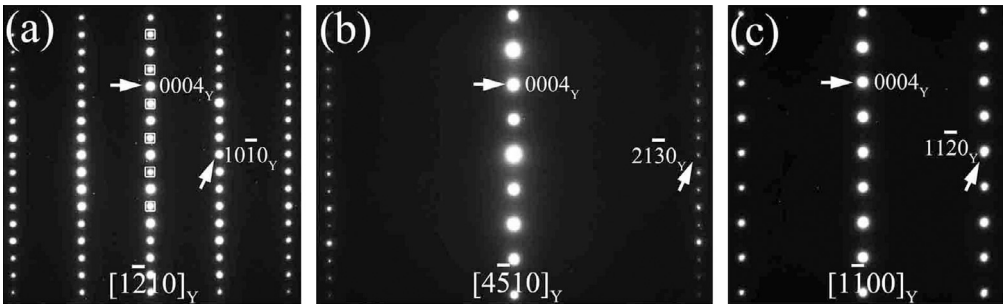

Fig. 3. A series EDPs of Y phase obtained by systematically tilting the crystal along $[0001]_Y$ crystallographic direction. The specific zone-axis is (a) $[1\bar{2}10]_Y$, (b) $[4\bar{5}10]_Y$, and (c) $[1\bar{1}00]_Y$. In (a), parts of the secondary diffraction spots which result from dynamic effect are highlighted by the square frames.

However, in the $[1\bar{2}10]_Y$ EDP, all vanished reflections appear because of dynamic diffraction. Detailed analysis of the structural characteristics for $P6_3/mmc$ space group is given in the literatures [30,31]. Moreover, it is worthwhile to point out here that based on our experimental observations as shown in Figs. 1 and 2a, the grains of hexagonal Y phase are in a shape of pancake which generally has a dimension of 10–20 nm in the $[0001]_Y$ crystallographic direction indicated by the hollow arrow, while 150–400 nm in the directions perpendicular to $[0001]_Y$.

3.2. Stacking faults in Y phase

To get the stacking sequence of Y phase, HRTEM was performed. Fig. 4a is the structural projection of Ti_2SC phase along the $[1\bar{2}10]_Y$ zone axis. The rectangle frame is the projection of a unit cell. It is obvious that the stacking sequence along $[0001]_Y$ direction for Ti_2SC can be described as

A B $\underline{\text{A}}$ B A $\underline{\text{B}}$ A (1)

The underlined letters denote the S layers while the others denote the Ti layers. The C atoms occupy the octahedral interstitial sites of Ti atoms and are not shown in this representation. Note that the S atoms in Ti_2SC nestle in the prismatic coordination polyhedron (B $\underline{\text{A}}$ B or A $\underline{\text{B}}$ A) formed by Ti atoms. Moreover, the S layers occupy the symmetrical position for adjacent Ti–C–Ti layers in the projected image. Actually, these stacking characteristics are similar to that of Ti_2AlC phase [32]. Fig. 4b HRTEM of Y phase projected along the $[1\bar{2}10]_Y$ crystallographic direction was obtained from the standard heat treated samples. The characteristic for the stacking sequence of Y phase is displayed vividly. Based on the image simulation and related structural projection shown as the down and up insets in Fig. 4b, the vertical lines represent the S layers, which are symmetrical positions for adjacent Ti–C–Ti layers indicated by the diagonal lines.

According to the structural projection drawing in Fig. 4a, it is known that there are two Ti layers and one C layer, namely one Ti_2C (Ti–C–Ti) layer between two S layers in Ti_2SC phase. This feature suggests a special kind of stacking fault in Ti_2SC, which is generated by the insertion of one or more Ti–C layers into the perfect Ti_2SC structure. Fig. 4c HRTEM of Y phase imaging from the $[1\bar{2}10]_Y$ direction reveals the special stacking fault with its corresponding structural projection shown in Fig. 4d. The stacking sequence for the stacking fault can be described as

A B $\underline{\text{A}}$ B A C′ B′ $\underline{\text{C}}$ B (2)

For clearly displaying the stacking alternation, sequence (1) and (2) are compared as follows:

A B $\underline{\text{A}}$ B A $\underline{\text{B}}$ A B
A B $\underline{\text{A}}$ B A C′ B′ $\underline{\text{C}}$ B (3)

It is seen that the above stacking fault formed by insertion of two Ti–C layers (denoted by C' and B') into the normal stacking sequence. Meanwhile, because of the insertion of two Ti–C layers,

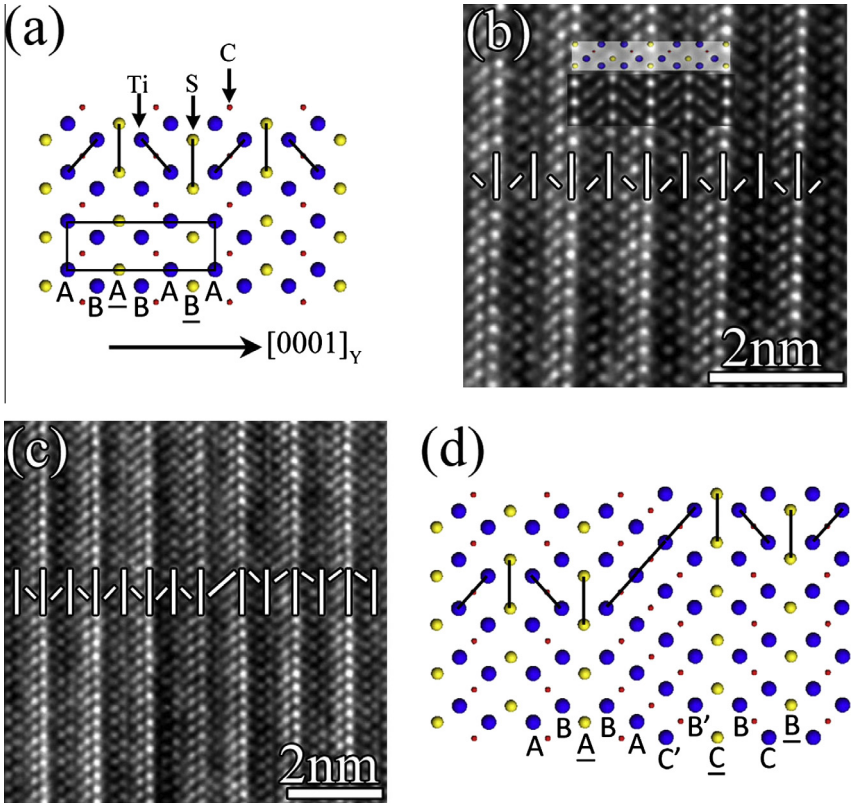

Fig. 4. (a) Structural projection of Y-Ti_2SC phase along $[1\bar{2}10]_Y$ direction. The down-pointing arrows indicate layers of Ti, S and C. Black diagonal lines highlight that S layer occupies the symmetrical layer in the projected image. The rectangle frame shows a structural unit of Ti_2SC and the horizontal arrow exhibits the $[0001]_Y$ direction, (b) HRTEM of the perfect Ti_2SC is imaging from $[1\bar{2}10]_Y$ direction. The upper inset is the structural projection. The lower inset corresponds to the simulated image with the thickness of 7 nm and focus value of 70 nm. The vertical lines represent the S layers and the diagonal lines represent the Ti–C–Ti layers, (c) HRTEM image of the stacking fault (SF) with two Ti–C layers inserted into Ti_2SC. The S layers are denoted by vertical lines, and (d) The structural schematic demonstrates the atomic occupation in the faulted structure given in (c).

the neighboring S layer changed its position from B to C. Note that S atoms at the stacking fault nestle in prismatic polyhedron (B′ C B) as in the perfect Ti_2SC. In addition, the cubic closed stacking sequences described as BAC′B′ forms at the stacking fault region. Both of these characteristics indicate that the above stacking fault possesses a lower energy.

3.3. Orientation relationship between Y phase and MC

It is known that X-ray diffraction (XRD) has limitation for the precipitated phase with minor content. However, in contrast to XRD, transmission electron microscopy is able to display morphological, crystallographic and compositional information from rather small domains as long as the interested microphase occurs in the observational field. Fig. 5a shows a mid-magnification TEM micrograph, which is obtained from the standard heat treated sample and projected along the $[1\bar{1}0]_{MC}$ direction. Based on the live Fast Fourier Transform (FFT) analysis (not supported here), the thin platelet indicated by an black downward-pointing arrow in Fig. 5a can be identified as the hexagonal Ti_2SC phase, which is embedded in the MC-type carbide with the boundary highlighted by dot line. Moreover, for this sandwiched structure, Ti_2SC phase does not run through the MC carbide. The width of the platelet is only about 10 nm, but the dimensions in the directions perpendicular to the width are approximate 150 nm. This indicates that the hexagonal layered Ti_2SC grew as two-dimensional thin film inside the cubic MC carbide.

In addition, Y phase maintains a fixed orientation relationship with the MC carbide. Fig. 5c displays the FFT result of the Fig. 5b HRTEM which corresponds to the sandwiched structure. The spots indicated by the hollow arrows can be indexed as the $[1\bar{1}0]_{MC}$ zone axis of cubic MC carbide. According to the composite EDPs shown in Fig. 5c, the orientation relationship between Y phase and MC can be determined as $[1\bar{2}10]_Y // [1\bar{1}0]_{MC}$ and $(0001)_Y // (111)_{MC}$, which agrees well with the speculation based on the crystallographic considerations for MC and Ti_2SC structure [23]. No other relationship independent of the above one can be observed between these two phases. Furthermore, besides the sandwiched structure, the side-by-side structure described in Fig. 2a also possesses the same orientation relationship. Actually, this intergrowth phenomenon has been already seen in other systems between MAX phases and carbides such as Ti_3SiC_2 platelets in the TiC matrix [33] and TiC platelets in the Ti_3AlC_2 matrix [31].

Based on the HRTEM of MC–Y–MC interface displaying in Fig. 5b, it can be seen that the thickness of the Y phase platelet of this section is about 10 nm, which implies an insertions of about nine unit cell thick Y phase into the $(111)_{MC}$ plane of MC carbide. The interface between MC carbide and Y phase is semi-coherent. Due to the variable numbers of Ti_2SC layers in the specific platelet, thickness of the Ti_2SC band is not always fixed, as seen in Fig. 5a. The reason for the variable width of the Y phase platelet will be given in the following section.

3.4. Interfacial structure between Y phase and MC

For convenience of the analysis, we only consider the interfacial structures between pure Ti_2SC and TiC without solution in the calculations. Fig. 6a–c shows three sets of possible projecting interfacial

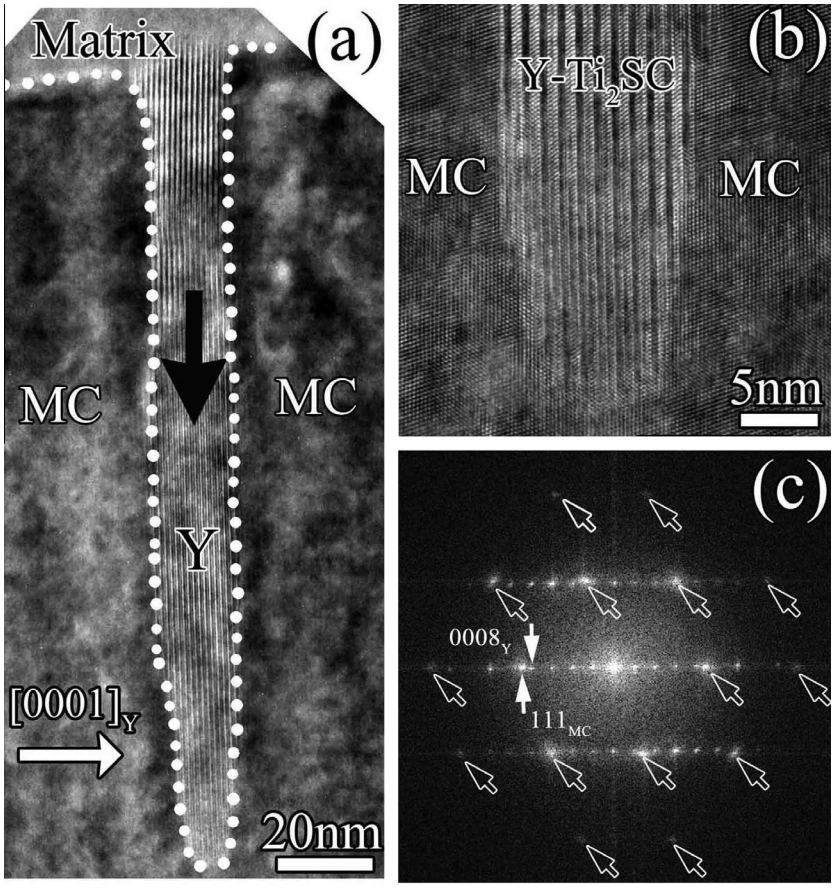

Fig. 5. (a) A mid-magnification image of the sandwiched structure composed of MC carbide and the Y-Ti_2SC phase. The down-pointing black arrow displays a slab shaped Y phase and the horizontal arrow shows the $[0001]_Y$ direction. The phase boundary between Y and MC is highlighted by the dot line, (b) HRTEM of the interface between Y phase and MC carbide, (c) The composite EDPs obtained by FFT of (b). The spots indicated by vertical up-arrow and down-arrow are indexed as $(1\,1\,1)_{MC}$ and $(0008)_Y$, respectively. Besides the indexed $(1\,1\,1)_{MC}$ reflection, the remnant spots for MC phase are indicated by the hollow arrows.

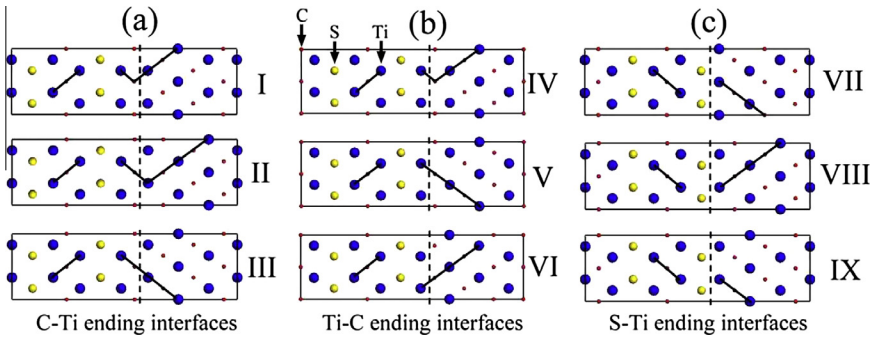

Fig. 6. Various models for interfacial structure of Ti_2SC and TiC along $[1\bar{2}10]_Y$ or $[1\bar{1}0]_{TiC}$ direction with (a) C–Ti ending including models I–III, (b) Ti–C ending including models IV–VI, (c) S–Ti ending including models VII–IX. The interface between Ti_2SC and TiC is highlighted by the vertical broken line. And in the vicinity of interface, the stacking of the bilateral Ti–C–Ti layers around the S layer is indicated by the diagonal lines. The Ti, S, C layers are indicated by the arrows.

structures of Ti_2SC/TiC along Ti_2SC $[1\bar{2}10]_Y$ direction with C–Ti, Ti–C and S–Ti bond ending, respectively. In each relaxed configuration, the interfacial energy between the two constituents is the dominant energy term. Table 1 lists the theoretical calculated interfacial energies for different models as shown in Fig. 6. It is found that interfacial energies of the models III, V and VIII are obviously lower than that of the other models in respective group. The interface between Ti_2SC and TiC is highlighted by the vertical broken lines as shown in Fig. 6. However, the Ti–C–Ti layer between S layers in Ti_2SC possesses very high similarity with that in TiC structure. Thus, on the

Table 1
Calculated interfacial energies of various Ti_2SC/TiC interface models as shown in Fig. 6.

Model	I	II	III	IV	V	VI	VII	VIII	IX
Interfacial energy (J/m^2)	2.4131	0.5404	0.1598	2.2982	0.1594	0.5271	1.0892	0.2026	0.6252

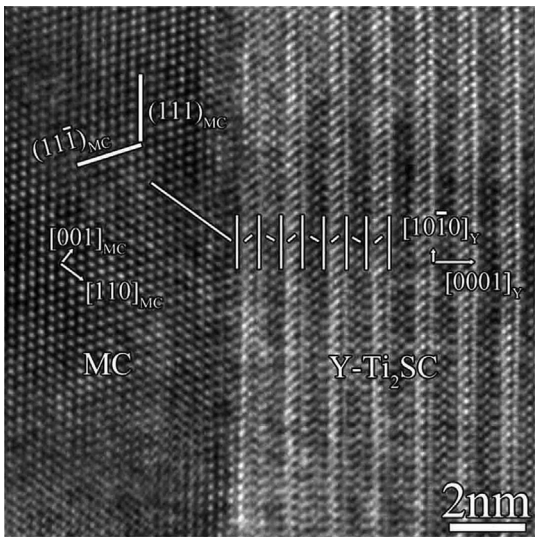

Fig. 7. The HRTEM image displays the interface of Y phase and MC carbide along $[1\bar{2}10]_Y$ direction. The vertical lines in Y phase indicate the location of S layers. The $\{111\}_{MC}$ planes, $[001]_{MC}$ and $[110]_{MC}$ directions for MC phase and $[10\bar{1}0]_Y$, $[0001]_Y$ directions for Y phase are all indicated.

whole, the models III, V and VIII have an equivalent interfacial structure with S layer as the symmetrical plane in the projected image. Fig. 7 HRTEM image taken along $[1\bar{2}10]_Y$ direction of Y phase displays that the most left Ti–C–Ti layer of Y phase and the most right M–C–M layer of MC carbide (denoted by an oblique line) are symmetrical about the S layer (denoted by a vertical line in Y phase) along the interface in the projected image, which agrees well with the above calculation. Since in the hexagonal structure of Ti_2SC, the local Ti–C bonding configuration is the same as that in cubic TiC carbide, it is reasonable that Ti_2SC thin platelets are frequently observed in TiC with the fixed orientation relationship. Moreover, as for the width variation of the Y phase shown in Fig. 5a, it should be attributed to the terraces along the interface of Y and MC carbide. Due to the low interfacial energy of symmetrical S layer terminated interfaces, the possible distance along $[0001]_Y$ direction between two terraces should be n^*d, where n represents integer and d represents the distance between two neighboring S layers along $[0001]_Y$ direction in Ti_2SC.

3.5. Compositional variation of Y phase during long-term annealing treatment

Fig. 8a dark field (DF) image (DF image obtained by using a coincident reflection from the area I and II) reveals two grains of Y phase with the nail-like shape, which precipitated independently in the matrix in the long-term annealing samples. Fig. 8b–d EDPs, which are acquired at the same tilting angle, corresponds to zones I, III and II indicated in Fig. 8a, respectively. Fig. 8b is the $[1\bar{2}10]_Y$ EDP of Y phase. And the Fig. 8d EDP can also be labeled as $[1\bar{2}10]_Y$ direction except for a 90° rotation compared with Fig. 8b EDP. On account of the composite EDPs obtained from zone III as shown in Fig. 8c, it can be easily determined that the nail-like morphology for Y phase is actually a 90° rotation twin structure along $[1\bar{2}10]_Y$ crystallographic direction. In other words, grain II should be regarded as a 90° rotation grain compared with grain I. Grain I contacts II with its basal plan $(0001)_Y$ which is rigid close-packed, thus the grain boundary is expected to have a lower energy. This phenomenon is similar to the large angle grain boundaries

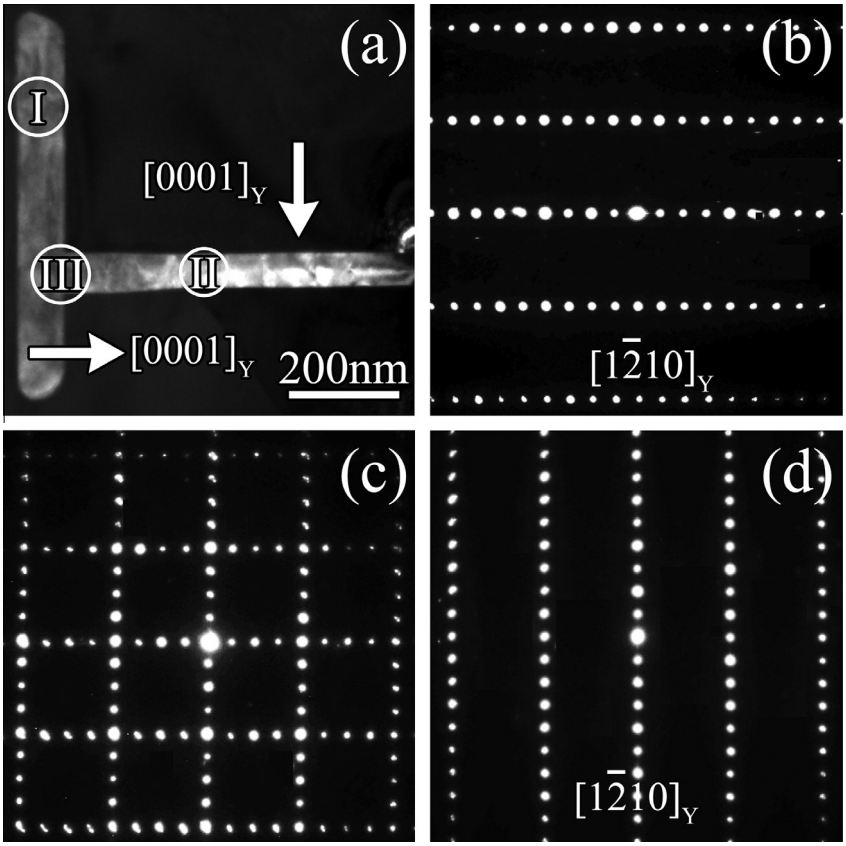

Fig. 8. (a) A low-magnification DF image reveals the Y phase with a nail-like morphology, which is obtained from long-term annealing samples. The arrows show the $[0001]_Y$ direction for each grain. (b)–(d) EDPs correspond to regions I, III, and II indicated in (a), respectively.

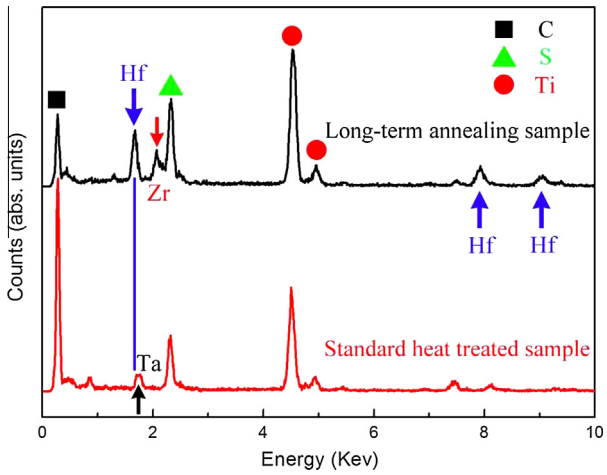

Fig. 9. EDS compositional comparison for Y phase precipitates in the standard heat treated samples (red profile) and the long-term annealing samples (black profile). (For interpretation of the references to colour in this figure legend, the reader is referred to the web version of this article.)

presented in Ti_3SiC_2 [34]. Moreover, the Y phase grain possesses no orientation relationship with the matrix.

By carefully indexing the $[1\bar{2}10]_Y$ EDPs, the lattice parameter of Y phase here can be calculated as $a = 0.34$ nm, $c = 1.21$ nm, where the parameter a preserves, but parameter c is 5.2% larger than that of the Y phase precipitated in the standard heat treated samples. To find the reason, EDS investigation was performed on the Y phase in the above two types of samples, respectively. It is found that the composition of Y phase here has evident difference from that in the samples only subjected to the standard heat treatment. From EDS profiles shown in Fig. 9, it can be clearly seen that the heavier elements Hf and Zr emerge and the trace element Ta disappears in the Y phase after the annealing treatment. Thus, partly substituting of Hf and Zr for Ti could be the reason for the increment of lattice parameter c. This is understandable considering the larger atomic radius for Zr and Hf in contrast to Ti atom. Furthermore, because of absorbing beneficial matrix elements of Hf and Zr during the long time annealing process, the existence of Y phase should be harmful for the superalloys.

4. Conclusions

We have carried out detailed microstructural investigations on the microphase Y-Ti_2SC precipitated in Ni-based superalloy. Some meaningful findings can be summarized as follows:

(1) In the standard heat treated samples, hexagonal Y-Ti_2SC phase ($P6_3/mmc$, $a = 0.33$ nm, $c = 1.15$ nm) is slab shaped. Meanwhile, the Y phase is always associated with MC carbide by forming either the sandwiched structure or the side-by-side structure. Besides that, stacking fault is found in Y phase, which can also be deemed as a structural unit slab of MC carbide. The crystallographic relationship between Y phase and MC can be derived as $[1\bar{2}10]_Y//[1\bar{1}0]_{MC}$ and $(0001)_Y//(111)_{MC}$.

(2) According to the calculated interfacial energies between Y phase and MC carbide, the interfacial structures with S-layer as the symmetrical plane in the $[1\bar{2}10]_Y$ projected image would possess the most stable configuration.

(3) In the long-term annealing samples, it is found that Y phase can solutionize amounts of beneficial elements Hf and Zr, which lead to a larger lattice parameter determined as $a = 0.34$ nm, $c = 1.21$ nm. Considering the absorption of beneficial elements, this solution phenomenon for Y phase is harmful for superalloys.

Acknowledgements

This work is supported by the National Basic Research Program of China (2009CB623705 and 2010CB631206). The authors are grateful to J. Wang for bulk sample preparation.

References

[1] Z.H. Xu, G.H. Huang, L.M. He, R.D. Mu, K. Wang, J.W. Dai, J. Alloys Comp. 586 (2014) 1–9.
[2] Y. Liu, K.Y. Chen, G. Lu, J.H. Zhang, Z.Q. Hu, Acta Mater. 45 (1997) 1837–1849.
[3] K. Chen, L.R. Zhao, J.S. Tse, Acta Mater. 51 (2003) 1079–1086.
[4] S. He, P. Peng, L. Peng, Y. Chen, H. Wei, Z.Q. Hu, J. Alloys Comp. 597 (2014) 243–248.
[5] P. Lortrakul, R.W. Trice, K.P. Trumble, M.A. Dayananda, Corros. Sci. 80 (2014) 408–415.
[6] Z.Q. Hu, W.R. Sun, S.R. Guo, Acta Metall. Sinica 9 (1996) 443–452.
[7] W.R. Sun, S.R. Guo, D.Z. Lu, Z.Q. Hu, Mater. Lett. 31 (1997) 195–200.
[8] K. Harris, J.B. Wahl, Mater. Sci. Technol. 25 (2009) 147–153.
[9] H.A. Chu, M.C. Young, H.C. Chu, L.W. Tsay, C. Chen, J. Mater. Eng. Perform. 23 (2014) 967–974.
[10] T. Gheno, D. Monceau, D. Oquab, Y. Cadoret, Oxid. Met. 73 (2010) 95–113.
[11] M. Chieux, C. Duhamel, R. Molins, F. Jomard, L. Remy, J.Y. Guedou, Oxid. Met. 81 (2014) 115–125.
[12] C. Sun, R.F. Huang, J.T. Guo, Z.Q. Hu, High Temp. Technol. 6 (1988) 145–148.
[13] M.W. Barsoum, MAX Phases: Properties of Machinable Ternary Carbides and Nitrides, Wiley VCH GmbH & Co., Weinheim, Germany, 2013. pp 16–17.
[14] M.W. Barsoum, Prog. Solid State Chem. 28 (2000) 201–281.
[15] T. Liao, J.Y. Wang, Y.C. Zhou, J. Mater. Res. 24 (2009) 556–564.
[16] Y.L. Du, Z.M. Sun, H. Hashimoto, Physica B 405 (2010) 720–723.
[17] S.X. Cui, W.X. Feng, H.Q. Hu, Z.B. Feng, H. Liu, Scripta Mater. 61 (2009) 576–579.
[18] S.R. Kulkarni, R.S. Vennila, N.A. Phatak, S.K. Saxena, C.S. Zha, T. El-Raghy, M.W. Barsoum, W. Luo, R. Ahuja, J. Alloys Comp. 448 (2008) L1–L4.
[19] W.B. Zhu, J.H. Song, B.C. Mei, J. Alloys Comp. 566 (2013) 191–195.
[20] S. Amini, M.W. Barsoum, T. El-Raghy, J. Am. Ceram. Soc. 90 (2007) 3953–3958.
[21] T.H. Scabarozi, S. Amini, P. Finkel, O.D. Leaffer, J.E. Spanier, M.W. Barsoum, M. Drulis, H. Drulis, W.M. Tambussi, J.D. Hettinger, S.E. Lofland, J. Appl. Phys. 104 (2008) 033502.
[22] S.R. Kulkarni, M. Merlini, N. Phatak, S.K. Saxena, G. Artioli, S. Amini, M.W. Barsoun, J. Alloys Comp. 469 (2009) 395–400.
[23] W. Wallace, R.T. Holt, T. Terada, Metallography 6 (1973) 511–526.
[24] G. Kresse, J. Furthmuller, Comp. Mater. Sci. 6 (1996) 15–50.
[25] G. Kresse, J. Furthmüller, Phys. Rev. B 54 (1996) 11169–11186.
[26] P.E. Blochl, Phys. Rev. B 50 (1994) 17953–17979.
[27] G. Kresse, D. Joubert, Phys. Rev. B 59 (1999) 1758–1775.
[28] J.P. Perdew, K. Burke, Phys. Rev. Lett. 77 (1996) 3865–3868.
[29] H.J. Monkhorst, J.D. Pack, Phys. Rev. B 13 (1976) 5188–5192.
[30] S. Arunajatesan, A.H. Carim, Mater. Lett. 20 (1994) 319–324.
[31] X.L. Ma, Y.L. Zhu, X.H. Wang, Y.C. Zhou, Philos. Mag. 84 (2004) 2969–2977.
[32] Z.J. Lin, M.J. Zhuo, Y.C. Zhou, M.S. Li, J.Y. Wang, Acta Mater. 54 (2006) 1009–1015.
[33] Y.C. Zhou, Z.M. Sun, Mater. Res. Innovat. 3 (2000) 286–291.
[34] R. Yu, Q. Zhan, L.L. He, Y.C. Zhou, H.Q. Ye, Philos. Mag. Lett. 83 (2003) 325–331.